

# Phonon anharmonicity of rutile TiO<sub>2</sub> studied by Raman spectrometry and molecular dynamics simulations

Tian Lan,\* Xiaoli Tang, and Brent Fultz

*Department of Applied Physics and Materials Science, California Institute of Technology, Pasadena, California 91125, USA*

(Received 29 January 2012; published 27 March 2012)

Raman spectra of rutile titanium dioxide (TiO<sub>2</sub>) were measured at temperatures from 100 to 1150 K. Each Raman mode showed unique changes with temperature. Beyond the volume-dependent quasiharmonicity, the explicit anharmonicity was large. A new method was developed to fit the thermal broadenings and shifts of Raman peaks with a full calculation of the kinematics of three-phonon and four-phonon processes, allowing the cubic and quartic components of the anharmonicity to be identified for each Raman mode. A dominant role of phonon-phonon kinematics on phonon shifts and broadenings is reported. Force-field molecular dynamics calculations with the Fourier-transformed velocity autocorrelation method were also used to perform a quantitative study of anharmonic effects, successfully accounting for the anomalous phonon anharmonicity of the  $B_{1g}$  mode.

DOI: [10.1103/PhysRevB.85.094305](https://doi.org/10.1103/PhysRevB.85.094305)

PACS number(s): 63.20.-e, 63.20.kg, 78.30.-j

## I. INTRODUCTION

Rutile is the most common and stable crystal structure of titanium dioxide (TiO<sub>2</sub>), and is important for both science and technology. Owing to its high refractive index and strong ultraviolet resistance, it is used extensively for pigments, optical coatings, and sunscreens. In the past two decades, TiO<sub>2</sub> surfaces have been subjects of research as photocatalysts and high efficiency solar cells.<sup>1-5</sup> Many questions remain about point defects, vibrational dynamics, size effects, and the recently reported close relationship between surface and bulk properties.<sup>5-7</sup> A better understanding of the lattice dynamics of rutile will help answer many of them.

Rutile TiO<sub>2</sub> is tetragonal with the space group  $P4/mnm$ . It is stable to 1800 K.<sup>8</sup> The other two naturally occurring phases of TiO<sub>2</sub>, anatase and brookite, are metastable and both convert to rutile upon heating. The 15 optical vibrational modes of rutile TiO<sub>2</sub> have the irreducible representation  $1A_{1g} + 1A_{2g} + 1A_{2u} + 1B_{1g} + 1B_{2g} + 2B_{1u} + 1E_g + 3E_u$ . The modes of symmetry  $B_{1g}$ ,  $E_g$ ,  $A_{1g}$ , and  $B_{2g}$  are Raman active. The Raman-active modes comprise motions of anions with respect to stationary central cations, either perpendicular to the  $c$  axis (modes  $B_{1g}$ ,  $A_{1g}$ , and  $B_{2g}$ ), or along the  $c$  axis (mode  $E_g$ ). The Raman spectrum of rutile was first recorded by Narayanan,<sup>9</sup> and peak assignments were made by Porto *et al.*<sup>10</sup> Raman spectrometry has been used in many studies of the lattice dynamics, phase transition, and nanostructures of TiO<sub>2</sub>.<sup>11-16</sup>

The present work on rutile TiO<sub>2</sub> focuses on anharmonicity, one of the most important but poorly understood characteristics of lattice dynamics at elevated temperatures. Anharmonic behavior affects crystal stability, heat capacity, optical properties, and thermal transport. It causes shifts of phonon energies with temperature because larger thermal displacements emphasize components of the potential with higher powers of the displacement. Phonon broadening from decreased lifetimes is another anharmonic phenomenon, and an anharmonic model should be able to predict both the broadenings and shifts of the phonons with temperature. To date there have been few studies of anharmonicity of rutile TiO<sub>2</sub>. Perhaps the most complete experimental results are from Samara and Peercy's work in 1973.<sup>11</sup> They reported frequency shifts of Raman modes with temperature and pressure, although the temperature range was

below 500 K and no broadening information was reported. Their results show that the  $B_{1g}$  mode, which comprises rotatory motions of the four nearest-neighbor oxygen anions around a central titanium atom (Fig. 1), is especially interesting. Its frequency changes little with temperature, but softens with pressure. Studies on other materials with the rutile structure, e.g., SnO<sub>2</sub>, MgF<sub>2</sub>, and FeF<sub>2</sub> report similar behavior of the  $B_{1g}$  mode.<sup>17-20</sup> There are two conflicting views on the physical origin of these anomalies. One attributes it to an incipient structural phase transition,<sup>17,21,22</sup> and the other attributes it to a thermal- or pressure-induced lattice contraction.<sup>18-20</sup>

Lattice dynamics calculations based on density functional theory (DFT) were used to study the effect of pressure on phonons in rutile TiO<sub>2</sub>.<sup>22,23</sup> These calculations were for low temperature and in the quasiharmonic approximation, where phonons are assumed to be harmonic but their frequencies change with volume. Only a few studies have used molecular dynamics (MD) to calculate anharmonic frequency shifts and broadenings of phonon mode of materials<sup>24,25</sup> and, to our knowledge, no such investigation has yet been performed on rutile TiO<sub>2</sub>.

Here we report measurements of Raman spectra with high resolution at temperatures from 100 to 1150 K. Both phonon frequency shifts and broadenings were measured and analyzed. The quasiharmonic effects from thermal expansion were separated from anharmonic effects of phonon-phonon interactions by comparing temperature- and pressure-dependent trends of the Raman peaks. To identify the effects of cubic and quartic anharmonicity, we developed a new anharmonic analysis that allows data fitting with calculated two-phonon kinematic functionals. We also used force-field molecular dynamics (MD) calculations and Fourier-transformed velocity autocorrelation function methods to study the anharmonicity. The methods proved quite successful, and are able to account for the anomalous phonon softening of the  $B_{1g}$  mode.

## II. EXPERIMENT

Samples were commercial TiO<sub>2</sub> powder (Alfa Aesar, Ward Hill, MA) with a rutile phase fraction of at least 99.9%. The sample powder was packed loosely inside a quartz sample

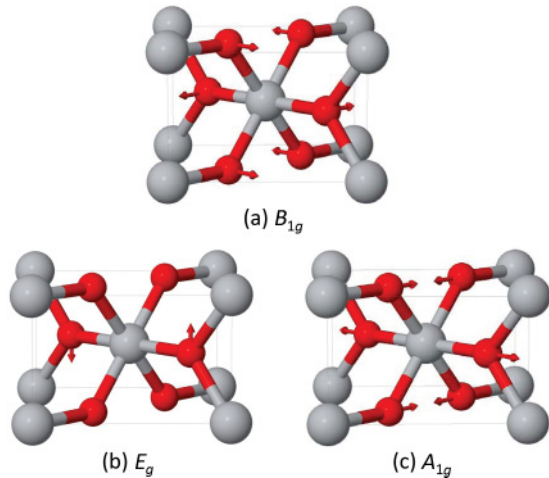


FIG. 1. (Color online) Rutile structure and oxygen atom displacements for Raman-active modes.

cell in a furnace with several electrical resistance heating elements insulated by ceramic rods.<sup>26</sup> The heating assembly was supported by stainless steel flanges and surrounded by heat shields made of niobium foil. The assembly was mounted in a quartz optical tube of 1 mm thickness, and evacuated with a turbomolecular pump. Both the interior and exterior of the tube were covered by aluminum foil for thermal radiation shielding. A temperature controller drove a 1 kW direct current power supply for heating power. For low-temperature measurements, the sample cell was mounted on the copper cold finger of a liquid nitrogen filled cryostat and evacuated. Uniformity of sample temperature was confirmed by multiple ultrafine thermocouples mounted at different locations inside the sample cell, and the temperature resolution was  $\pm 1$  K. Samples were measured at temperatures from 100 to 1150 K, with intervals of 100 K below 700 K and 50 K above 700 K.

The Raman spectrometer used the 532 nm line from a solid-state laser at power levels of 100 mW or less. A high efficiency long pass edge filter was used to block the laser line. The single pass spectrometer (Princeton Instruments Acton Series 500 mm) used a two-dimensional charge-coupled device camera with thermoelectric cooling (Princeton Instruments PIXIS 400 B). The instrument resolution was  $1.4 \text{ cm}^{-1}$ . Each Raman spectrum was accumulated in 10 measurements with 1 s exposure times.

### III. MOLECULAR DYNAMICS CALCULATIONS

Our classical molecular dynamics (MD) calculations used simulation tools in the GULP software package.<sup>27</sup> Rutile  $\text{TiO}_2$ , with its relatively small ionicity and large dipole moments on anions, is a challenging system for developing an interatomic potential. Few of those we tried<sup>28–31</sup> could simultaneously provide the crystal structure, elastic properties, thermal expansion, and phonon vibrational frequencies. The best results for phonon properties were obtained with the Buckingham potential (Model 3) developed by Mostoller and Wang (MW shell model).<sup>31</sup> The MW shell model was parameterized by fitting the phonon spectra over the whole Brillouin zone, and the model also gives reasonable bulk properties. We altered

slightly this model to improve its transferability and stability at different temperatures and pressures (the shell charge of titanium atoms was increased to  $0.37|e|$ ). The parameters of the force-field model were fixed for all the calculations presented below.

To extract anharmonic information on individual phonon modes from the atomic trajectories of the MD simulations, the phonon spectral energy density function  $g(\vec{q}, \omega)$  was obtained by the velocity autocorrelation technique<sup>32,33</sup>

$$g(\vec{q}, \omega) = \int dt e^{-i\omega t} \sum_{n,b} e^{i\vec{q} \cdot \vec{R}_n} \langle \vec{v}_{n,b}(t) \vec{v}_{0,0}(0) \rangle, \quad (1)$$

where  $\langle \rangle$  is an ensemble average,  $\vec{v}_{n,b}(t)$  is the velocity of the atom  $b$  in the unit cell  $n$  at time  $t$ ,  $\vec{R}_n$  is the equilibrium position of the cell  $n$ , and  $\vec{q}$  is the phonon wave vector. Equation (1) is both a time and space Fourier transform, and gives the frequency and lifetime of each phonon mode with a resolution determined by the size of the supercell used in the simulation.

Our MD simulations were performed with a  $2 \times 2 \times 20$  supercell containing 960 atom cores and shells. We used the Verlet algorithm, an  $N$ - $P$ - $T$  ensemble, and a modified Nosé-Hoover thermostat for control of temperature and pressure. Both the isobaric temperature-dependent phonon peaks and the isothermal pressure-dependent phonon peaks were obtained in ranges of 300 to 900 K and 0 to 6 GPa. The run time for each set was 100 ps with time steps of 0.5 fs and sampling periods of 10 fs. The time-dependent atomic trajectories of velocity were postprocessed by the velocity autocorrelation method to

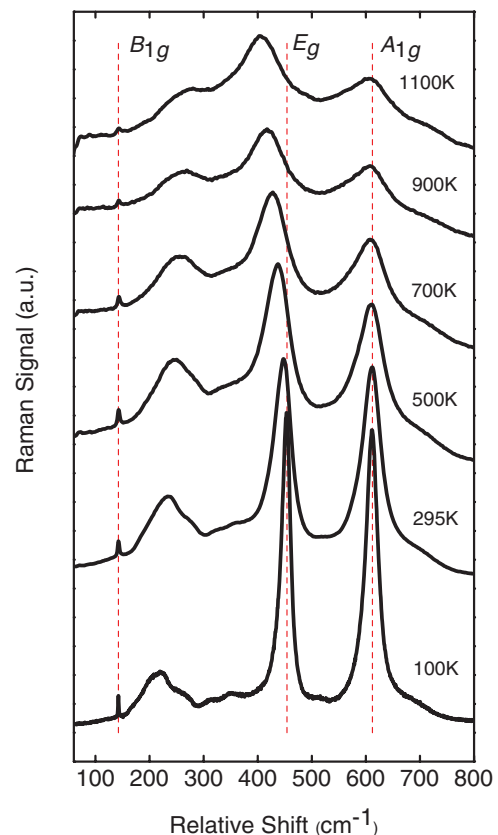


FIG. 2. (Color online) Raman spectra of rutile  $\text{TiO}_2$  at selected temperatures from 100 to 1150 K.

obtain mode frequencies and linewidths. The resolution of the wave vector  $\vec{q}$  along the  $\Gamma$ -Z direction was therefore  $k_z/20$ , where  $k_z$  is the magnitude of the reciprocal lattice vector. The frequency resolution was approximately  $0.5 \text{ cm}^{-1}$ .

## IV. RESULTS

### A. Experiment

Representative Raman spectra are shown in Fig. 2. Three of the four Raman active modes,  $B_{1g}$ ,  $E_g$ , and  $A_{1g}$ , have enough intensity for extracting quantitative information on phonon frequencies and linewidths. The strong high-order Raman band around  $235 \text{ cm}^{-1}$  is also observed clearly, consistent with the results of Porto, Fleury, and Damen.<sup>10</sup> Mode  $B_{2g}$  proved too weak for obtaining quantitative information (and is even difficult to resolve at low temperature with polarized Raman scattering<sup>10,11</sup>).

After background subtraction, each peak in each spectrum was fitted to a Lorentzian function to obtain a centroid and full width at half maximum (FWHM). The FWHM data from the experiment were corrected for the finite resolution of the spectrometer.<sup>34</sup> Figure 3 presents these results of peak shifts and widths versus temperature. At room temperature, the Raman peak frequencies were  $143 \text{ cm}^{-1}$ ,  $447 \text{ cm}^{-1}$ , and  $612 \text{ cm}^{-1}$ , consistent with the well-accepted data from Porto, Fleury, and Damen.<sup>10</sup> We also find good agreement with the frequency shift data reported by Samara and Peercy<sup>11</sup> at temperatures below 480 K.

The  $E_g$  mode undergoes a large phonon softening with temperature. The  $A_{1g}$  mode has a small thermal softening at high temperature, but below 400 K the  $A_{1g}$  mode tends to stiffen slightly with temperature, as also reported by Samara

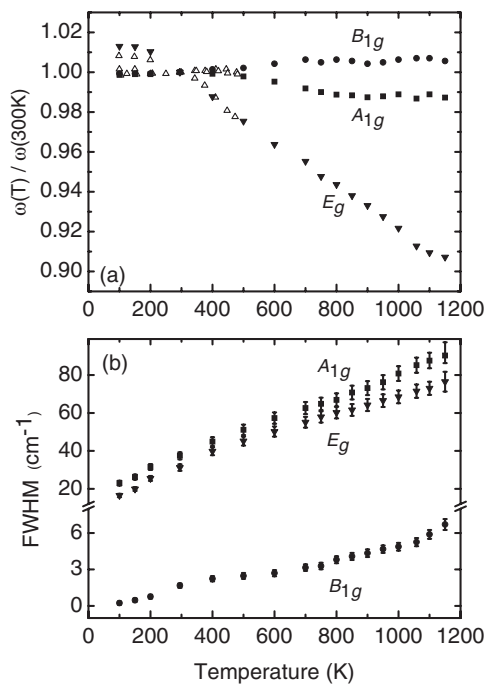


FIG. 3. Temperature dependence of (a) frequency shifts, (b) FWHM, of the Raman modes  $B_{1g}$ ,  $E_g$ , and  $A_{1g}$ . Data of Ref. 11 are shown as open triangles in panel (a).

TABLE I. Properties of rutile TiO<sub>2</sub> from present calculations, compared to experimental data. Units: lattice parameters in Å, Raman frequencies in  $\text{cm}^{-1}$ , thermal expansion coefficients in  $10^{-6} \text{ K}^{-1}$ , and volume compressibility in  $10^{-3} \text{ GPa}^{-1}$ .

	Experiment <sup>a</sup>	Calculation
Crystal structure		
$a$	4.593	4.499
$c$	2.959	3.077
$u$	0.3048	0.3059
Raman frequency		
$B_{1g}$	143	169
$E_g$	447	400
$A_{1g}$	612	558
$B_{2g}$	826	803
Thermal expansion		
$\beta_a$	8.25	8.13
$\beta_b$	10.86	9.85
$\beta_v$	27.35	26.1
Compressibility		
$\kappa$	4.73	4.09

<sup>a</sup>Crystal structure data are from Ref. 35, Raman frequencies are from measurements in the present work, thermal expansion data are from Ref. 36, and compressibility data are from Ref. 11.

and Peercy.<sup>11</sup> The  $B_{1g}$  mode appears to have no thermal shift. The thermal broadenings of  $E_g$  and  $A_{1g}$  peaks are large, but the  $B_{1g}$  mode shows far less broadening.

### B. MD simulations

Table I presents results from our MD simulations and experimental data on lattice parameters, Raman frequencies, thermal expansion, and volume compressibility. The calculated lattice parameters and Raman frequencies were from MD simulations at 300 K. The thermal expansion and compressibility were from isobaric (0 GPa) MD calculations to 900 K and isothermal (300 K) MD calculations to 6 GPa. The agreement with experimental data is good. The good agreement for the thermal expansion is encouraging for the use of the MD calculations for predicting anharmonic behavior.

Figure 4(a) presents simulated Raman peaks of the  $B_{1g}$  mode at elevated temperatures at 0 GPa, and at elevated pressures at 300 K. The small thermal shift and broadening seen in the experimental results of Fig. 2 are apparent in the simulated results. Figures 4(b) and 4(c) present simulated Raman peaks of the  $E_g$  and  $A_{1g}$  modes at elevated temperature. The large thermal broadening of both modes and the large thermal shift of the  $E_g$  mode are in apparent agreement with the experimental results of Fig. 2.

## V. EXPERIMENTAL DATA ANALYSIS

### A. Analysis of quasiharmonicity and anharmonicity

Both quasiharmonicity and explicit anharmonicity contribute to the nonharmonic lattice dynamics of rutile TiO<sub>2</sub>. In the quasiharmonic model, phonon modes behave harmonically with infinite lifetimes, but their frequencies are changed by the effects of volume on the interatomic potential. Explicit anharmonicity originates with phonon-phonon interactions, which increase with temperature. Explicit anharmonicity

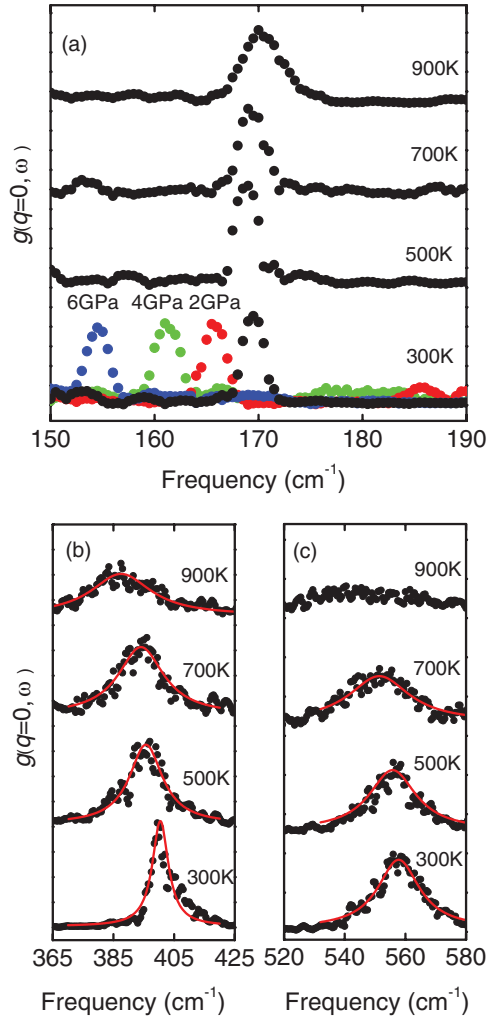


FIG. 4. (Color online) (a)  $B_{1g}$  Raman peak calculated from the velocity trajectories of MD simulations, at temperatures as labeled and constant pressure of 0 GPa, and at pressures from 0 to 6 GPa at 300 K. (b) Calculated  $E_g$  Raman peak, and (c) calculated  $A_{1g}$  Raman peak at temperatures as labeled and constant pressure of 0 GPa. Solid red curves are the Lorentzian fits.

contributes to shifts in phonon frequencies, but also causes phonon damping and lifetime broadening of phonon peaks with temperature. The large peak broadenings and peculiar differences in shifts of the Raman peaks in rutile  $\text{TiO}_2$  suggest there are important effects from explicit anharmonicity.

To separate the effects of quasiharmonicity and explicit anharmonicity, we treat the mode frequency  $\omega_j = \omega_j(V, T)$  as a function of volume and temperature<sup>11</sup>

$$\left(\frac{\partial \ln \omega_j}{\partial T}\right)_p = -\frac{\beta}{\kappa} \left(\frac{\partial \ln \omega_j}{\partial P}\right)_T + \left(\frac{\partial \ln \omega_j}{\partial T}\right)_V, \quad (2)$$

where  $j$  is the phonon mode index,  $\beta$  is the volume thermal expansivity, and  $\kappa$  is the isothermal compressibility. The left-hand side gives the temperature-dependent isobaric frequency shift, including both quasiharmonic and explicit anharmonic behavior. The first term on the right-hand side, the isothermal frequency shift as a function of pressure, is the quasiharmonic contribution to the frequency shift. By defining a mode Grüneisen parameter as the proportionality of the relative

change of the mode frequency to the relative change of volume, i.e.,  $\gamma_j = -\partial(\ln \omega_j)/(\partial(\ln V))$ , this term can be written as  $\gamma_j \beta$ . The second term on the right of Eq. (2) is the pure temperature contribution to the frequency shift from the explicit anharmonicity. From the difference of the isobaric and isothermal frequency shifts, the explicit anharmonicity can be determined experimentally.

We used the mode Grüneisen parameters  $\gamma_j$  reported by Samara and Peercy<sup>11</sup> from Raman measurements under pressure. Since the  $\gamma_j$  are very weakly dependent on temperature,<sup>11,17</sup> as is the thermal expansion above 300 K,<sup>36</sup> the  $\gamma_j$  can be assumed to be constants for identifying the volume-dependent quasiharmonic contribution. The results, summarized in Table II, separate the frequency shifts from quasiharmonicity and explicit anharmonicity. Samara and Peercy's results at 296 K are also shown for comparison. For the  $B_{1g}$  mode, Table II shows that the quasiharmonic and explicit anharmonic contributions are both large but opposite in sign, and their near-perfect cancellation causes the  $B_{1g}$  mode to have a small thermal frequency shift to 1150 K. The quasiharmonic softening of the  $B_{1g}$  mode with increasing pressure (or, equivalently, with decreasing temperature) and its negative Grüneisen parameter are anomalous. The  $A_{1g}$  mode has a similar cancellation of quasiharmonic and explicit anharmonic contributions, but the signs of two contributions are reversed. The positive explicit anharmonic shift of the  $A_{1g}$  mode is unusual. We find this explicit anharmonicity at higher temperatures to be smaller than Samara and Peercy's result below 400 K. There is a similar difference for the  $E_g$  mode but with an opposite trend, where the explicit anharmonic contribution increases by an order of magnitude when averaged over a larger range of temperature. It becomes comparable to the quasiharmonic contribution, hastening the softening of the  $E_g$  mode at temperatures above 400 K.

## B. Analysis of cubic and quartic anharmonicity

The previous section showed how the comparison of temperature-dependent and pressure-dependent shifts of phonon frequencies can be used to separate quasiharmonic and anharmonic behavior. The anharmonic behavior can be resolved further. When phonon anharmonicities are treated as perturbations that cause interactions of quasiharmonic phonons, it is known how the cubic anharmonicity associated with three-phonon processes and the quartic anharmonicity of four-phonon processes affect differently the shift and broadening of quasiharmonic phonons. The Feynman diagrams for the leading-order contributions to the phonon self-energy are<sup>37</sup>

$$\Sigma_j = \Sigma^{(3)} + \Sigma^{(3')} + \Sigma^{(4)}, \quad (3a)$$

$$\Sigma_j = \begin{array}{c} \vec{q}_1 \\ \circlearrowleft \\ \vec{q}_j \quad \vec{q}_j \\ \circlearrowright \\ \vec{q}_2 \end{array} + \begin{array}{c} -\vec{q}_2 \\ \circlearrowleft \\ \vec{q}_j \quad \vec{q}_j \\ \circlearrowright \\ \vec{q}_1 \end{array} + \begin{array}{c} -\vec{q}_1 \\ \circlearrowleft \\ \vec{q}_j \quad \vec{q}_j \\ \circlearrowright \\ \vec{q}_1 \end{array}. \quad (3b)$$



TABLE II. Frequencies of the three Raman modes, their logarithmic pressure and temperature derivatives, and mode Grüneisen parameters. The measured isobaric temperature derivatives are separated into the pure volume and pure temperature contributions. Samara and Peercy's results are listed in the lower row for each mode.

Mode	$\omega$ (cm <sup>-1</sup> )	$\gamma_j$	$\left(\frac{\partial \ln \omega}{\partial T}\right)_P$ (10 <sup>-5</sup> K <sup>-1</sup> )	=	$-\gamma_j \beta^a$ (10 <sup>-5</sup> K <sup>-1</sup> )	+	$\left(\frac{\partial \ln \omega}{\partial T}\right)_V$ (10 <sup>-5</sup> K <sup>-1</sup> )
$B_{1g}$	143	-5.03	0.788		11.82		-11.03
	143		0.6			-11.22	
$E_g$	447	2.43	-11.17		-5.71		-5.46
	450		-6.3			-0.59	
$A_{1g}$	612	1.59	-1.42		-3.72		2.3
	612		0.6			4.32	

<sup>a</sup>Mode Grüneisen parameters are from Ref. 11.

The lowest-order contributions to the shifts,  $\Delta$ , and broadenings,  $\Gamma$ , of the Raman mode  $j$  are derived from the real and imaginary parts of the cubic and quartic self-energies  $\Sigma^{(3)}$ ,  $\Sigma^{(3*)}$ , and  $\Sigma^{(4)}$ ,

$$\Delta^{(3)}(j; \Omega) = -\frac{18}{\hbar^2} \sum_{\vec{q}_1 j_1} \sum_{\vec{q}_2 j_2} |V(j; \vec{q}_1 j_1; \vec{q}_2 j_2)|^2 \times \wp \left[ \frac{n_1 + n_2 + 1}{\Omega + \omega_1 + \omega_2} - \frac{n_1 + n_2 + 1}{\Omega - \omega_1 - \omega_2} + \frac{n_1 - n_2}{\Omega - \omega_1 + \omega_2} - \frac{n_1 - n_2}{\Omega + \omega_1 - \omega_2} \right], \quad (4a)$$

$$\Delta^{(3*)}(j) = -\frac{72}{\hbar^2} \sum_{j_1} \sum_{\vec{q}_2 j_2} V(j; j; \vec{0} j_1) V(\vec{0} j_1; -\vec{q}_2 j_2; \vec{q}_2 j_2) \times \wp \left( \frac{1}{\omega_1} \right) \left( n_2 + \frac{1}{2} \right), \quad (4b)$$

$$\Delta^{(4)}(j) = \frac{24}{\hbar} \sum_{\vec{q}_1 j_1} V(j; j; \vec{q}_1 j_1; -\vec{q}_1 j_1) \left( n_1 + \frac{1}{2} \right), \quad (4c)$$

$$\Gamma^{(3)}(j; \Omega) = \frac{18\pi}{\hbar^2} \sum_{\vec{q}_1 j_1} \sum_{\vec{q}_2 j_2} |V(j; \vec{q}_1 j_1; \vec{q}_2 j_2)|^2 \times [(n_1 + n_2 + 1)\delta(\Omega - \omega_1 - \omega_2) + 2(n_1 - n_2)\delta(\Omega + \omega_1 - \omega_2)], \quad (4d)$$

where  $\Omega$  is the phonon frequency and  $\wp$  denotes the Cauchy principal part. The  $V()$ 's are elements of the Fourier-transformed anharmonic tensor, denoting the coupling strength between the Raman mode  $j$  to other modes  $\{\vec{q}_i j_i\}$  having quasiharmonic frequencies  $\{\omega_i\}$  and occupancies  $\{n_i\}$ . The broadening of the Raman peaks is  $2\Gamma^{(3)}(j; \Omega)$ . The simplicity of the first-order shift  $\Delta^{(4)}(j; \Omega)$  is partly a consequence of zero momentum transfer in Raman spectroscopy.

For crystals having atoms without inversion symmetry, as is the case for the rutile structure, an additional low-order cubic term  $\Delta^{(3*)}(j)$ , expressed in Eq. (4b), is possible. It corresponds to the second diagram in Eq. (3) with instantaneous phonons at a three-phonon vertex.<sup>37</sup> Group theory further showed that the only nonzero contribution to Eq. (4b) arises from the  $j_1$  mode that belongs to the identity representation.<sup>38</sup> Owing to the rigorous restrictions on the existence of instantaneous three-phonon processes,  $\Delta^{(3*)}$  is generally much smaller than  $\Delta^{(3)}$ .

For rutile TiO<sub>2</sub>, this term needs to be evaluated only for the  $A_{1g}$  mode because it does not have inversion symmetry for oxygen atom motions [see Fig. 1(c)].

Including all shifts, the frequencies of the Raman peaks are

$$\omega_j(T, \Omega) = \omega_{j0} \exp \left[ -\gamma_j \int_0^T \beta(T) dT \right] + \Delta^{(3)}(j; \Omega) + \Delta^{(3*)}(j) + \Delta^{(4)}(j). \quad (5)$$

The first term on the right of Eq. (5) is the integral form of the quasiharmonic phonon shift [discussed after Eq. (2)] and from the last term of Eq. (5),  $(\partial \omega_j / \partial T)_V \delta T = \Delta^{(3)}(j; \Omega) + \Delta^{(3*)}(j) + \Delta^{(4)}(j)$  is the explicit anharmonic shift. To obtain  $\beta(T)$ , experimental data from 4 to 1200 K<sup>11,36</sup> were fitted with a well-accepted analytical form<sup>39</sup>

$$\beta(T) = \left( \frac{A}{T} + \frac{B}{T^2} \right) \sinh^{-2} \left( \frac{T_1}{T} \right) \quad (6)$$

giving  $A = 7.16 \times 10^{-5}$ ,  $B = 0.524$  K, and  $T_1 = 146.2$  K.

In what follows, we use Eqs. (4a)–(4d) to identify the magnitudes and signs of the cubic and quartic anharmonicities from the thermal shifts and broadenings of the Raman modes in rutile TiO<sub>2</sub>. We do not calculate the  $V()$ 's, which are complicated tensor quantities, but instead we treat them as parameters in fitting the experimental trends of the Raman modes. We do a full calculation of the two-phonon density of states, however, as described below.

From Ipatova *et al.*,<sup>40</sup> an anharmonic tensor element for a process with  $s$  phonons is

$$V(j; \vec{q}_1 j_1; \dots; \vec{q}_{s-1} j_{s-1}) = \frac{1}{2s!} \left( \frac{\hbar}{2N} \right)^{\frac{s}{2}} N \Delta(\vec{q}_1 + \dots + \vec{q}_{s-1}) \times [\omega_{j_0} \omega_1 \dots \omega_{s-1}]^{\frac{1}{2}} C(j; \vec{q}_1 j_1; \dots; \vec{q}_{s-1} j_{s-1}), \quad (7)$$

where  $\Delta(\vec{q}_1 + \dots + \vec{q}_{s-1})$  enforces momentum conservation. Ipatova *et al.*<sup>40</sup> suggest that the  $C()$ 's are slowly varying functions of their arguments. Several studies used this assumption to calculate or fit approximately the anharmonic broadening.<sup>40–42</sup> Klemens assumed the frequency-independent part of the coupling tensor for a Raman mode  $j$  was a constant that depended on the strain field of the mode.<sup>43</sup> Likewise, we consider the term  $C(j; \vec{q}_1 j_1; \dots; \vec{q}_{s-1} j_{s-1})$  to be a constant of the Raman mode  $j$ , and we use it as a fitting parameter. This

approximation is not rigorous because  $C(j; \vec{q}_1 j_1; \vec{q}_2 j_2)$  and  $C(j; j; \vec{q}_1 j_1; -\vec{q}_1 j_1)$  change with  $j_1$  and  $j_2$ , but an average over modes,  $\langle C \rangle = \sum_{1,2} C(j; \vec{q}_1 j_1; \vec{q}_2 j_2) / \sum_{1,2} 1$ , is found by the fitting, where 1, 2 under the summation symbol represent  $\vec{q}_i j_i$ . We define the cubic and quartic fitting parameters as

$$C_j^{(3)} = \langle C(j; \vec{q}_1 j_1; \vec{q}_2 j_2) \rangle, \quad (8a)$$

$$C_j^{(4)} = \langle C(j; j; \vec{q}_1 j_1; -\vec{q}_1 j_1) \rangle. \quad (8b)$$

While the anharmonic tensor describes the coupling strength of phonon-phonon interactions, a prerequisite is that the phonons in these processes satisfy the kinematical conditions of conservation of energy and momentum [as explicitly written in Eqs. (4) and (7)]. Central to phonon linewidth broadening from the cubic anharmonicity,  $2\Gamma^{(3)}$ , is the two-phonon density of states (DOS),  $D(\Omega)$ , defined as

$$\begin{aligned} D(\Omega) &= \sum_{\vec{q}_1, j_1} \sum_{\vec{q}_2, j_2} D(\Omega, \omega_1, \omega_2) \\ &= \frac{1}{N} \sum_{\vec{q}_1, j_1} \sum_{\vec{q}_2, j_2} \Delta(\vec{q}_1 + \vec{q}_2) [(n_1 + n_2 + 1) \delta(\Omega - \omega_1 - \omega_2) \\ &\quad + 2(n_1 - n_2) \delta(\Omega + \omega_1 - \omega_2)], \end{aligned} \quad (9)$$

which depends on temperature through the phonon occupancy factors,  $n$ . The first and second terms in square brackets in Eq. (9) are from down-conversion and up-conversion processes, respectively.<sup>44</sup> The two-phonon kinematical functional for the anharmonic frequency shifts from the cubic anharmonicity,  $\Delta^{(3)}$ , is  $P(\Omega)$ ,

$$\begin{aligned} P(\Omega) &= \sum_{\vec{q}_1, j_1} \sum_{\vec{q}_2, j_2} P(\Omega, \omega_1, \omega_2) \\ &= \frac{1}{N} \sum_{\vec{q}_1, j_1} \sum_{\vec{q}_2, j_2} \Delta(\vec{q}_1 + \vec{q}_2) \wp \left[ \frac{n_1 + n_2 + 1}{\Omega + \omega_1 + \omega_2} \right. \\ &\quad \left. - \frac{n_1 + n_2 + 1}{\Omega - \omega_1 - \omega_2} + \frac{n_1 - n_2}{\Omega - \omega_1 + \omega_2} - \frac{n_1 - n_2}{\Omega + \omega_1 - \omega_2} \right]. \end{aligned} \quad (10)$$

Both  $D(\Omega)$  and  $P(\Omega)$  were calculated at various temperatures for the phonon dispersions calculated with the MW shell model, sampling  $\omega_{\vec{q}j}$  with a  $16 \times 16 \times 16$   $q$ -point grid, giving good convergence. Figure 5 shows representative results for  $D(\Omega)$  and  $P(\Omega)$ . The down-conversion and up-conversion subspectra of  $D(\Omega)$  are shown for 1000 K. The up-conversion processes are skewed to lower frequencies, and disappear above  $800 \text{ cm}^{-1}$ , consistent with the highest phonon frequency of rutile  $\text{TiO}_2$  being about  $800 \text{ cm}^{-1}$ .

With Eqs. (7), (8), (9), and (10), the anharmonic frequency shifts and linewidth broadenings are rewritten as functions of  $P(\Omega)$  and  $D(\Omega)$ , weighted by average anharmonic coupling strengths,

$$\Delta^{(3)}(j; \Omega) = -\frac{\hbar}{64} \omega_{j0} |C_j^{(3)}|^2 \sum_{\vec{q}_1, j_1} \sum_{\vec{q}_2, j_2} \omega_1 \omega_2 P(\Omega, \omega_1, \omega_2), \quad (11a)$$

$$\Delta^{(3)}(j) = -\frac{\hbar}{16N} \omega_{j0} |C_j^{(3)}|^2 \sum_{\vec{q}_2, j_2} \omega_{j_2}(\vec{q}_2) \left( n_{\vec{q}_2, j_2} + \frac{1}{2} \right), \quad (11b)$$

$$\Delta^{(4)}(j) = \frac{\hbar}{8N} \omega_{j0} C_j^{(4)} \sum_{\vec{q}_1, j_1} \omega_{j_1}(\vec{q}_1) \left( n_{\vec{q}_1, j_1} + \frac{1}{2} \right), \quad (11c)$$

$$\Gamma^{(3)}(j; \Omega) = \frac{\pi \hbar}{64} \omega_{j0} |C_j^{(3)}|^2 \sum_{\vec{q}_1, j_1} \sum_{\vec{q}_2, j_2} \omega_1 \omega_2 D(\Omega, \omega_1, \omega_2). \quad (11d)$$

It is an approximation to use the same  $|C_j^{(3)}|^2$  for  $\Delta^{(3)}$  and  $\Delta^{(3)}$ , but  $\Delta^{(3)}$  is expected to be small, and is nonzero for only the  $A_{1g}$  mode. Using Eq. (11) and Eq. (5) for each Raman mode, both its frequency shift and its broadening were fitted simultaneously with the two parameters,  $|C_j^{(3)}|^2$  and  $C_j^{(4)}$ . The best fits for the shifts and broadenings are shown in Figs. 6, 7, and 8, and the fitting parameters are given in Table III. Figures 6(a), 7(a), and 8(a) also present contributions to the shift from the quasiharmonic and explicit anharmonicity as dashed curves.

## VI. DISCUSSION

### A. Anharmonicities from experimental trends

Two factors determine the explicit anharmonicity—the anharmonic coupling strength described by the coupling tensor and the two-phonon kinematical processes described by  $D(\Omega)$  and  $P(\Omega)$ . The two are approximately separable if the anharmonicity tensor does not vary significantly for different phonon processes, and some features of the fits of Figs. 6, 7, and 8 suggest this is approximately true. Figure 5 shows that  $D(\Omega)$  has a peak at the frequency  $\Omega_0 = 600 \text{ cm}^{-1}$ . The cubic

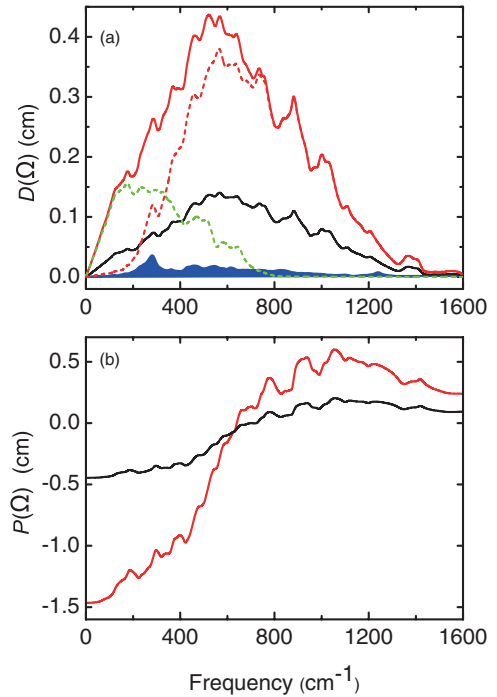


FIG. 5. (Color online) (a) Two-phonon density of states  $D(\Omega)$  of Eq. (9) for 300 K (black) and 1000 K (red). The up-conversion and down-conversion contributions to  $D(\Omega)$  at 1000 K are shown in green dash and red dash curves, respectively. The overtone process at 1000 K is highlighted as the filled area under the blue curve. (b)  $P(\Omega)$  of Eq. (10) at 300 K (black) and 1000 K (red).

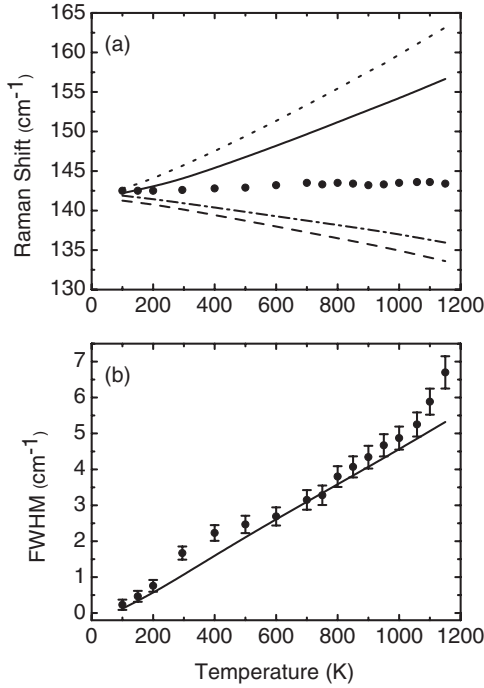


FIG. 6. Temperature dependence of parameters for fittings to Raman peaks of mode  $B_{1g}$  (a) frequency shift, and (b) FWHM. Solid circles are experimental data. Solid curves are the fittings of the experimental points to Eq. (5) and Eq. (11d). Dotted line is the quasiharmonic contribution to the frequency shift. Dash-dot line is the explicit anharmonicity  $\omega_0 + \Delta^{(4)} + \Delta^{(3)}$ , and dashed line is  $\omega_0 + \Delta^{(3)}$ .

anharmonicity and hence the broadening of the mode  $E_g$  and especially  $A_{1g}$  are large because they are near this peak in  $D(\Omega)$ . On the other hand, the  $B_{1g}$  mode can have only a small cubic anharmonicity because its frequency is far from  $\Omega_0$ . For the  $E_g$  and  $A_{1g}$  modes good fittings to the broadenings are obtained, indicating the dominance of cubic anharmonicity. The unusual concave downward curvature of broadening of  $E_g$  in Fig. 3(b) is caused by the large frequency shift of this mode with temperature, which rapidly moves the  $E_g$  mode away from  $\Omega_0$ , and down the steep slope of  $D(\Omega)$  in Fig. 5. This causes the broadening of the  $E_g$  mode to have a trend with temperature that is less than linear.

Starting with the same cubic fitting parameters used for the broadenings, the frequency shifts of the  $E_g$  and  $A_{1g}$  modes are fit well by adding the quasiharmonic and quartic anharmonic effects. As illustrated in Fig. 7 and Fig. 8, the quartic contribution  $\Delta^{(4)}$  is of the same order as the cubic one  $\Delta^{(3)}$ , consistent with the fact that  $\Delta^{(4)}$  and  $\Delta^{(3)}$  are both the leading order terms for the anharmonic frequency shifts. They are opposite in sign, however, because  $\Delta^{(3)}$  enters with a negative sign times the square of the cubic coupling tensor. The net anharmonic shift is usually negative, as for the  $E_g$  mode. For the  $A_{1g}$  mode, the additional contribution from the instantaneous three-phonon processes,  $\Delta^{(3)}$ , is also considered, but owing to a symmetry restriction, this term is small. The  $A_{1g}$  mode is unusual, having a net anharmonic shift that is positive, indicating the quartic contribution to the shift is larger than the cubic. Figure 5 shows that, at the frequency

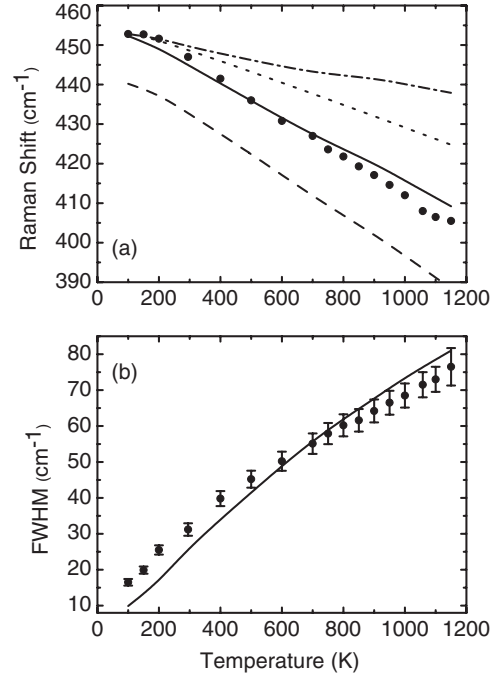


FIG. 7. Temperature dependence of parameters for fittings to Raman peaks of mode  $E_g$  (a) frequency shift, and (b) FWHM. Dotted line is the quasiharmonic contribution to the frequency shifts. Dash-dot line is the explicit anharmonicity  $\omega_0 + \Delta^{(4)} + \Delta^{(3)}$  and dashed line is  $\omega_0 + \Delta^{(3)}$ .

of mode  $A_{1g}$ ,  $P(\Omega)$  is close to zero. The cubic anharmonic shift  $\Delta^{(3)}$  is therefore attenuated for the  $A_{1g}$  mode.

For the  $B_{1g}$  mode, Fig. 6(a) shows that the fitting deviates substantially from the experimental data. The discrepancies may originate with anharmonic contributions beyond the leading terms we considered. The rapid increase of the linewidth of the  $B_{1g}$  mode above the Debye temperature ( $\simeq 780$  K for rutile TiO<sub>2</sub>) further supports this argument (a  $T^2$  dependence is typical of broadening from higher-order quartic anharmonicity<sup>40</sup>).

The ratio of cubic to quartic anharmonicity is sometimes evaluated by fitting Raman spectra to a simplified Klemens model, in which the shifts and broadenings from phonon-phonon interactions [Eq. (4)] include only overtone processes (one optical phonon at the  $\Gamma$  point decays into two or three phonons of equal energy on the same branch).<sup>45</sup> In this simplified model, the temperature dependence of the Raman peak linewidth is

$$\Gamma_j(T) = \Gamma_j(0) + A \left( 1 + \frac{2}{e^{\hbar\omega_{j0}/2k_B T} - 1} \right) + B \left( 1 + \frac{3}{e^{\hbar\omega_{j0}/3k_B T} - 1} + \frac{3}{(e^{\hbar\omega_{j0}/3k_B T} - 1)^2} \right), \quad (12)$$

where  $\Gamma_j(0)$  is the FWHM extrapolated to 0 K, and  $A$  and  $B$  are fitting parameters for three-phonon and four-phonon processes, respectively. A similar expression is used to fit the frequency shift, with fitting parameters  $C$ ,  $D$  replacing  $A$ ,  $B$ , and the quasiharmonic frequency shift replacing  $\Gamma_j(0)$  in Eq. (12). This approach often gives good fits to experimental

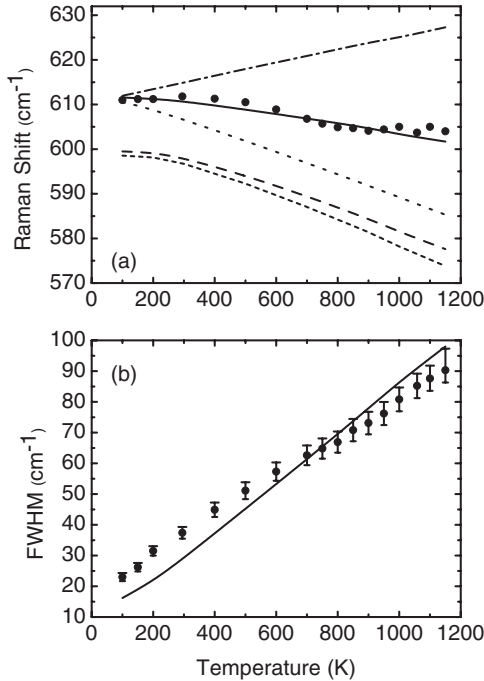


FIG. 8. Temperature dependence of parameters for fittings to Raman peaks of mode  $A_{1g}$  (a) frequency shift, and (b) FWHM. Dotted line represents the quasi-harmonic contribution to the frequency shifts. Dash-dot line is the explicit anharmonicity  $\omega_0 + \Delta^{(4)} + \Delta^{(3)} + \Delta^{(3')}$ , short dash line corresponds to  $\omega_0 + \Delta^{(3)} + \Delta^{(3')}$ , and dashed line is  $\omega_0 + \Delta^{(3)}$ .

Raman data, but the results can be misleading owing to the oversimplified approximations. In performing such fits for our data on rutile  $\text{TiO}_2$ , we found a cubic anharmonicity for the  $B_{1g}$  mode that was large compared to the quartic, which we know to be incorrect. This approach also gave a negative fitting parameter  $B$  for the quartic anharmonicity to explain the concave curvature of the thermal broadening of the  $E_g$  mode, which is unreasonable. The independent fits to thermal trends of linewidth and frequency shift [using Eq. (12) and its equivalent] offer no correlation between these quantities, even though they share a dependence on the same cubic anharmonic coupling tensor. Furthermore, it has been shown that the contributions from overtone processes are usually very small,<sup>34</sup> as is shown by the lowest curve in Fig. 5(a) for rutile  $\text{TiO}_2$ .

### B. Anharmonicities from MD simulations

Figure 9 shows the effects of temperature on the frequency shifts and broadenings of the  $B_{1g}$  mode, obtained from MD results such as those of Fig. 4(a). Also shown is the effect of pressure on the frequency shift of the  $B_{1g}$  mode. These results

TABLE III. Fitting parameters for the temperature dependent Raman modes (unit:  $10^{11} \text{ erg}^{-1}$ ).

	$B_{1g}$	$E_g$	$A_{1g}$
$ C^{(3)} ^2$	0.21	0.63	0.34
$C^{(4)}$	0.45	3.0	2.4

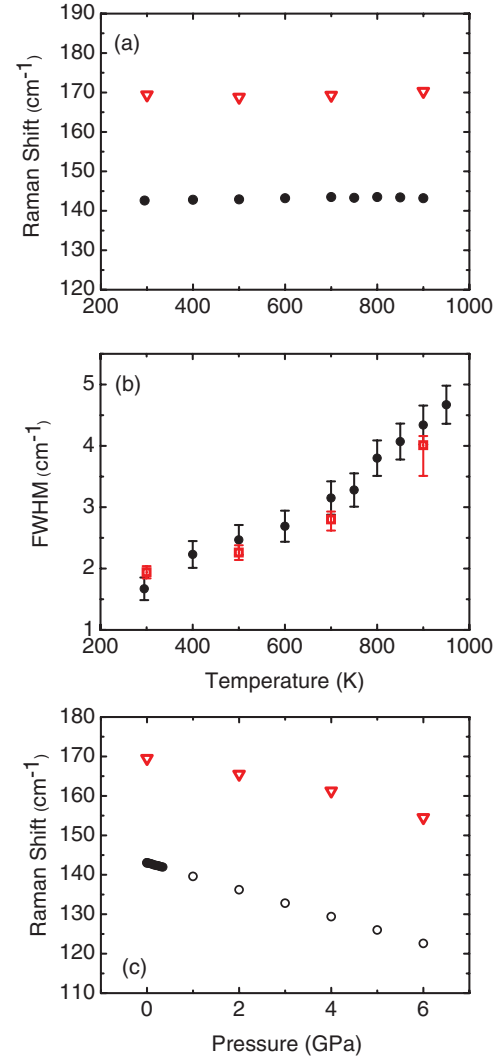


FIG. 9. (Color online) (a) Temperature-dependent frequency shift, (b) FWHM broadening, and (c) pressure-dependent frequency shift, of the  $B_{1g}$  mode from MD calculations (red), compared with experimental data (black).

are in excellent agreement with the experimental data. From Fig. 9(c), the Grüneisen parameter of the  $B_{1g}$  mode is found to be  $-4.23$ , which compares well to the experimental value of  $-5.03$  reported by Samara and Peercy.<sup>11</sup>

To further study the anomalous anharmonicity of the  $B_{1g}$  mode, the frozen phonon method was used with the force field of MW shell model, allowing us to obtain the effective potential energy curve of the  $B_{1g}$  mode at different temperatures and pressures, as shown in Fig. 10. Three sets of lattice parameters were used, obtained from MD calculations at 300 K and 0 GPa, 300 K and 6 GPa, and 800 K and 0 GPa. These correspond to the volume at ambient conditions, a volume contraction of about 2.4%, and a volume expansion by about 1.3%, respectively. The quadratic potential dominates, and there is no cubic anharmonic contribution, as expected from symmetry. The quartic anharmonic potential is significant, however.

Figure 10 shows that the harmonic part of the  $B_{1g}$  potential has a curvature that increases with volume, contrary to



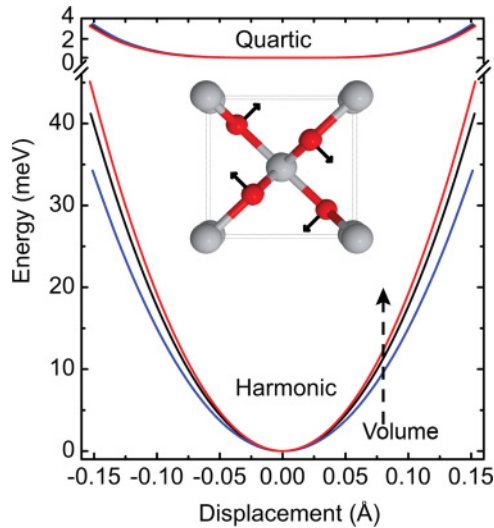


FIG. 10. (Color online) Frozen phonon potential of the  $B_{1g}$  mode calculated with the MW shell model, and its response to the volume increase (indicated as the dash arrow). The potential is decomposed into the harmonic component and quartic component. The three potentials are for lattice parameters corresponding to 300 K at 0 GPa (black), 300 K at 6 GPa (blue), and 800 K at 0 GPa (red). The inset shows the  $B_{1g}$  mode of rutile TiO<sub>2</sub> structure projected along the  $c$  axis. Small arrows indicate the polarization vectors of this mode.

the usual trend. This anomalous quasiharmonic response to volume reduces the force constant with increasing pressure, giving an anomalous mode softening. This phenomenon can be explained by the transverse motion of oxygen anion in the  $B_{1g}$  mode, perpendicular to the Ti-O bond. This transverse motion makes the mean interatomic distance  $\langle R \rangle = |\langle \vec{r}_O - \vec{r}_{Ti} \rangle|$  greater than the distance between the mean atomic positions  $R_0 = |\langle \vec{r}_O \rangle - \langle \vec{r}_{Ti} \rangle|$ . An increase in volume increases the tension in the bond, tending to bring  $\langle R \rangle$  closer to  $R_0$ . The restoring force for transverse motion is thus increased, and the mode is stiffened.<sup>46</sup> For most materials, this tension effect is hardly seen because the stretching along the bond direction is usually dominant, and bond stretching weakens the force constant. Rutile TiO<sub>2</sub> is special owing to its open structure, which reduces the coordination of atoms around the oxygen, allowing it large transverse amplitudes. Moreover, the Ti-O bonds are stiff (vibrational modes along this bond direction, such as mode  $B_{2g}$ , are at the highest frequencies). The rigidity of the Ti-O bond suppresses bond stretching for the  $B_{1g}$  mode. A similar mechanism was used to explain the negative thermal expansion in polyethylene and Cu<sub>2</sub>O.<sup>47,48</sup> The temperature dependence of the  $B_{1g}$  mode is also anomalous—for both experiment and MD calculations, thermal expansion does not stiffen or soften the mode. As discussed following Eq. (2), this results from a quartic anharmonicity that increases with temperature, canceling the stiffening trend from quasiharmonicity.

The success of the MD calculations at elevated temperature and pressure shows that a shell model with a Buckingham potential can reproduce both the anomalous quasiharmonicity and the explicit anharmonicity of the  $B_{1g}$  mode of rutile TiO<sub>2</sub>, giving a detailed picture than can be compared to results from uniaxial-stress experiments,<sup>49</sup> zero-pressure extrapolations of phonon frequencies,<sup>19,20</sup> and DFT calculations within the

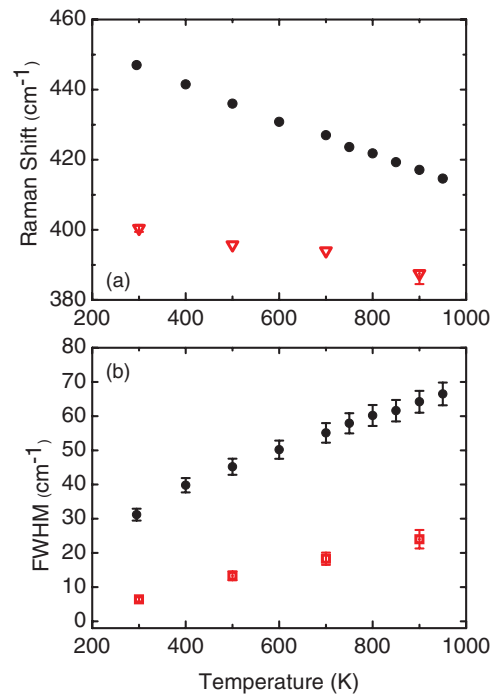


FIG. 11. (Color online) Temperature dependence of the (a) frequency shift, and (b) FWHM broadening, of the  $E_g$  mode from MD simulations (red) and experimental data (black).

quasiharmonic approximation.<sup>22</sup> No orthorhombic or other distortion was found for our supercell at any temperature or pressure. The anomalous anharmonic behavior of the  $B_{1g}$  mode can be explained by volume effects on quasiharmonic force constants, and by the quartic anharmonicity. We need not invoke an incipient phase transition to the orthorhombic structure to explain this anharmonic behavior.

For the  $E_g$  and  $A_{1g}$  modes, the force field of the MW shell model qualitatively accounts for the large anharmonicity. As shown in Fig. 11 and Fig. 12, we obtain the trends of the large linewidth broadenings and the thermal softening of the  $E_g$  mode, but the MD calculations significantly underestimate the amount. The  $E_g$  and  $A_{1g}$  modes are more anharmonic than predicted by the MW shell model.

For each Raman mode, Fig. 13 compares the anharmonic potential to the harmonic potential, both obtained from the frozen phonon method with the MW shell model. The  $B_{1g}$  mode shows a large quartic potential. The  $A_{1g}$  mode is dominated by cubic anharmonicity. (A cubic contribution is not allowed by symmetry for the  $B_{1g}$  and  $E_g$  modes.) Since the MW shell model significantly underestimates the anharmonicity of the  $A_{1g}$  mode, the actual cubic potential energy could be larger. Evidently the frozen phonon potential cannot itself explain the large anharmonic effects, especially for the  $E_g$  mode, due to the fact that the frozen phonon potential does not account for phonon-phonon interactions. The large anharmonic effects of the  $E_g$  mode may originate from the many couplings between anharmonic phonons.

### C. Vibrational entropy of rutile TiO<sub>2</sub>

Vibrational entropy is important for thermophysical properties of materials, and for the thermodynamic stabilities of

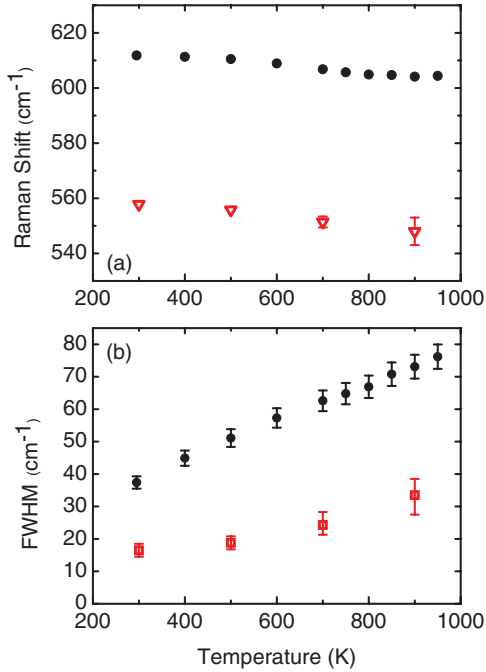


FIG. 12. (Color online) Temperature dependence of the (a) frequency shift, and (b) FWHM broadening, of the  $A_{1g}$  mode from MD simulations (red) and experimental data (black).

different solid phases as reviewed recently.<sup>50</sup> The vibrational entropy  $S_{\text{vib}}$  is

$$S_{\text{vib}} = 3k_B \int_0^{\infty} g(\epsilon) [(n(\epsilon) + 1) \ln(n(\epsilon) + 1) - n(\epsilon) \ln(n(\epsilon))] d\epsilon, \quad (13)$$

where  $g(\epsilon)$  is the single phonon DOS at the temperature of interest, and  $n(\epsilon)$  is the phonon occupancy. Although Eq. (13) is derived from the harmonic model, it is known to be valid for anharmonic systems to first order in perturbation theory.<sup>51</sup> From the phonon DOS obtained by MD simulations at elevated temperatures,  $S_{\text{vib}}$  was calculated with Eq. (13) and the results are presented in Table IV. The calculated results are in general agreement with the experimental data, but the discrepancies

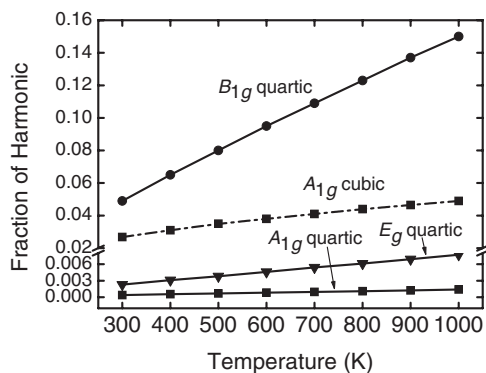


FIG. 13. Ratio of the mode anharmonic potential and harmonic potential, with increasing temperature.

TABLE IV. Entropy in J/(mol K) of rutile  $\text{TiO}_2$  from MD calculations and experimental data of Ref. 52.

$T$ (K)	MD	Experimental
300	48.01	50.69
500	80.28	82.21
700	101.79	105.51
900	119.22	123.65

suggest that the average phonon frequencies from the MD calculations are about 3.7% too small.

## VII. CONCLUSIONS

Raman spectra were measured on rutile  $\text{TiO}_2$  at temperatures to 1150 K, and giant anharmonic behaviors were found for the shifts and broadenings of the three measurable Raman peaks. The pressure dependence and temperature dependence of the Raman peak shifts were used to separate the anharmonic behavior from the quasiharmonic behavior. Individual assessments of the cubic and quartic contributions to the anharmonicity were performed with a new data fitting method based on the kinematics of three-phonon and four-phonon processes, with the phonons calculated from a shell model in this case. In fitting the anharmonic behavior, mode broadening is from effects of cubic anharmonicity, while the anharmonic shifts are from the same cubic factor plus a quartic anharmonicity. The quartic anharmonicity of the  $B_{1g}$  mode was found to be large, and its cubic anharmonicity small, unlike the large cubic anharmonicity found for the  $E_g$  and  $A_{1g}$  modes. From successes of the fitting method, we suggest that the observed anharmonic effects are dominated by considerations of the kinematics of energy and momentum conservation in the phonon-phonon scattering processes, and less by the details of the anharmonicity tensors.

Force-field molecular dynamics (MD) calculations were performed with the same shell model. Both the anomalous quasiharmonic behavior and the explicit anharmonic behavior of the  $B_{1g}$  mode from our calculations were in excellent agreement with the experimental observation. No orthorhombic distortion was found, suggesting that the anomalous anharmonicity originates with the phonon responses to temperature and pressure, and not an incipient phase transition. Discrepancies for the  $E_g$  and  $A_{1g}$  modes suggest that the shell model potential may not be sufficient for obtaining accurate anharmonicities from molecular dynamics calculations, however.

## ACKNOWLEDGMENTS

We thank George R. Rossman for important discussions and Chen W. Li for help with the furnace design. This work was supported by DOE BES under Contract No. DE-FG02-03ER46055. The work benefited from software developed in the DANSE project under NSF Grant No. DMR-0520547.

\*Corresponding author: tianlan@caltech.edu

- <sup>1</sup>A. L. Linsebigler, G. Lu, and J. T. Yates, *Chem. Rev.* **95**, 735 (1995).  
<sup>2</sup>U. G. Akpan and B. H. Hameed, *Appl. Catal. A-Gen.* **375**, 1 (2010).  
<sup>3</sup>Y. Du, N. A. Deskins, Z. Zhang, Z. Dohnálek, M. Dupuis, and I. Lyubinetsky, *Phys. Rev. Lett.* **102**, 096102 (2009).  
<sup>4</sup>B. O'Regan and M. Grätzel, *Nature (London)* **353**, 737 (1991).  
<sup>5</sup>U. Diebold, *Surf. Sci. Rep.* **48**, 53 (2003).  
<sup>6</sup>P. Balaya, *Energy Environ. Sci.* **1**, 645 (2008).  
<sup>7</sup>M. K. Nowotny, L. R. Sheppard, T. Bak, and J. Nowotny, *J. Phys. Chem. C* **112**, 5275 (2008).  
<sup>8</sup>D. G. Isaak, J. D. Carnes, O. L. Anderson, H. Cynn, and E. Hake, *Phys. Chem. Minerals* **26**, 31 (1998).  
<sup>9</sup>P. S. Narayanan, *Proc. Indian Acad. Sci. Sect. A* **32**, 279 (1950).  
<sup>10</sup>S. P. S. Porto, P. A. Fleury, and T. C. Damen, *Phys. Rev.* **154**, 522 (1967).  
<sup>11</sup>G. A. Samara and P. S. Peercy, *Phys. Rev. B* **7**, 1131 (1973).  
<sup>12</sup>U. Balachandran and N. G. Eror, *J. Solid State Chem.* **42**, 276 (1982).  
<sup>13</sup>L. G. Liu and T. P. Mernagh, *Eur. J. Mineral.* **4**, 45 (1992).  
<sup>14</sup>H. Chang and P. Huang, *J. Raman Spectrosc.* **29**, 97 (1998).  
<sup>15</sup>W. Zhang, Y. He, M. Zhang, Z. Yin, and Q. Chen, *J. Phys. D: Appl. Phys.* **33**, 912 (2000).  
<sup>16</sup>X. Feng, Y. Guo, J. Chen, and J. Zhang, *J. Biomater. Sci.-Polym. Ed.* **18**, 1443 (2007).  
<sup>17</sup>P. S. Peercy and B. Morosin, *Phys. Rev. B* **7**, 2779 (1972).  
<sup>18</sup>J. Pascual, J. Camassel, P. Merle, B. Gil, and H. Mathieu, *Phys. Rev. B* **24**, 2101 (1981).  
<sup>19</sup>A. Perakis, E. Sarantopoulou, Y. S. Raptis, and C. Raptis, *Phys. Rev. B* **59**, 775 (1999).  
<sup>20</sup>D. J. Lockwood, R. S. Katiyar, and V. C. Y. So, *Phys. Rev. B* **28**, 1983 (1983).  
<sup>21</sup>P. S. Peercy, *Phys. Rev. B* **8**, 6018 (1973).  
<sup>22</sup>B. Montanari and N. M. Harrison, *J. Phys.: Condens. Matter* **16**, 273 (2004).  
<sup>23</sup>P. D. Mitev, K. Hermansson, B. Montanari, and K. Refson, *Phys. Rev. B* **81**, 134303 (2010).  
<sup>24</sup>J. A. Thomas, J. E. Turney, R. M. Iutzi, C. H. Amon, and A. J. H. McGaughey, *Phys. Rev. B* **81**, 081411 (2010).  
<sup>25</sup>G. Kopidakis, C. Wang, C. M. Soukoulis, and K. Ho, *J. Phys.: Condens. Matter* **9**, 7071 (1997).  
<sup>26</sup>C. W. Li, M. M. McKerns, and B. Fultz, *Phys. Rev. B* **80**, 054304 (2009).  
<sup>27</sup>J. D. Gale and A. L. Rohl, *Mol. Simul.* **29**, 291 (2003).  
<sup>28</sup>M. Matsui and M. Akaogi, *Mol. Simul.* **6**, 239 (1991).  
<sup>29</sup>V. Swamy and J. D. Gale, *Phys. Rev. B* **62**, 5406 (2000).  
<sup>30</sup>G. C. Mather, M. S. Islam, and F. M. Figueiredo, *Adv. Func. Mater.* **17**, 905 (2007).  
<sup>31</sup>M. Mostoller and J. C. Wang, *Phys. Rev. B* **32**, 6773 (1985).  
<sup>32</sup>D. W. Noid, M. L. Koszykowski, and R. A. Marcus, *J. Chem. Phys.* **67**, 404 (1977).  
<sup>33</sup>C. Z. Wang, C. T. Chan, and K. M. Ho, *Phys. Rev. B* **42**, 11276 (1990).  
<sup>34</sup>J. Menéndez and M. Cardona, *Phys. Rev. B* **29**, 2051 (1984).  
<sup>35</sup>J. K. Burdett, T. Hughbanks, G. J. Miller, J. W. Richardson Jr., and J. V. Smith, *J. Am. Chem. Soc.* **109**, 3639 (1987).  
<sup>36</sup>C. M. B. Henderson, K. S. Knight, and A. R. Lennie, *Open Mineral J.* **3**, 1 (2009).  
<sup>37</sup>A. A. Maradudin and A. E. Fein, *Phys. Rev.* **128**, 2589 (1962).  
<sup>38</sup>J. L. Feldman, L. L. Boyer, P. J. Edwardson, and J. R. Hardy, *Phys. Rev. B* **40**, 4105 (1989).  
<sup>39</sup>E. Liarokapis, E. Anastassakis, and G. A. Kourouklis, *Phys. Rev. B* **32**, 8346 (1985).  
<sup>40</sup>I. P. Ipatova, A. A. Maradudin, and R. F. Wallis, *Phys. Rev.* **155**, 882 (1967).  
<sup>41</sup>K. Nishidate and T. Sato, *Phys. Rev. B* **46**, 13773 (1992).  
<sup>42</sup>J. Suda and T. Sato, *J. Phys. Soc. Jpn.* **66**, 1707 (1996).  
<sup>43</sup>P. G. Klemens, *Phys. Rev.* **148**, 845 (1966).  
<sup>44</sup>X. Tang, C. W. Li, and B. Fultz, *Phys. Rev. B* **82**, 184301 (2010).  
<sup>45</sup>M. Balkanski, R. F. Wallis, and E. Haro, *Phys. Rev. B* **28**, 1928 (1983).  
<sup>46</sup>G. D. Barrera, J. A. O. Bruno, T. H. K. Barron, and N. L. Allan, *J. Phys.: Condens. Matter* **17**, 217 (2005).  
<sup>47</sup>J. A. O. Bruno, N. L. Allan, T. H. K. Barron, and A. D. Turner, *Phys. Rev. B* **58**, 8416 (1998).  
<sup>48</sup>R. Mittal, S. L. Chaplot, S. K. Mishra, and P. P. Bose, *Phys. Rev. B* **75**, 174303 (2007).  
<sup>49</sup>P. Merle, J. Pascual, J. Camassel, and H. Mathieu, *Phys. Rev. B* **21**, 1617 (1980).  
<sup>50</sup>B. Fultz, *Prog. Mater. Sci.* **55**, 247 (2010).  
<sup>51</sup>D. C. Wallace, *Thermodynamics of Crystals* (Dover, New York, 1998), p. 235.  
<sup>52</sup>S. J. Smith, R. Stevens, S. Liu, G. Li, A. Navrotsky, J. Boerio-Goates, and B. F. Woodfield, *Am. Miner.* **94**, 236 (2009).